IEEE Access
Multidisciplinary : Rapid Review : Open Access Journal

Received 16 June 2023, accepted 2 July 2023, date of publication 10 July 2023, date of current version 19 July 2023.

Digital Object Identifier 10.1109/ACCESS.2023.3293847

RESEARCH ARTICLE

Polarization-Based Gigahertz Near-Field Bio-Sample Detector Prepared by Integrated-Passive-Device Fabrication

JIA-KANG WU[2], YING-YING JI[1], JUN-GE LIANG[1,2], YU-TING CHEN[2], CONG WANG[3], CHENG QIAN[4], YANG-FAN SUN[1], CAI-LI REN[1], AND SVETLANA VON GRATOWSKI[5]

[1]Wuxi Central Rehabilitation Hospital, The Affiliated Mental Health Center of Jiangnan University, Wuxi, Jiangsu 214151, China
[2]Engineering Research Center of IoT Technology Applications (Ministry of Education), Department of Electronic Engineering, Jiangnan University, Wuxi 214122, China
[3]School of Electronics and Information Engineering, Harbin Institute of Technology, Harbin 150001, China
[4]Zhejiang Laboratory, Hangzhou 311121, China
[5]Kotelnikov Institute of Radio Engineering and Electronics, Russian Academy of Science (IRE RAS), 125009 Moscow, Russia

Corresponding authors: Yang-Fan Sun (9862023084@jiangnan.edu.cn), Cai-Li Ren (rencaili@njmu.edu.cn), and Svetlana von Gratowski (svetlana.gratowski@yandex.ru)

This work was supported by the National Key Research and Development Program of China (2021YFA1401103), Postgraduate Research & Practice Innovation Program of Jiangsu Province (KYCX22_2301), 2022 Wuxi Taihu Talent Program: Innovative Leading Talent Team (1096010241230120).

ABSTRACT Far-field detection has been widely used in biomedical diagnosis, security inspection, such as MRI, ultrasonic, SPECT, X-ray, etc. However, the near-field detection has yet to be well established. This paper proposed a sensor structure with series inductance and capacitor. The inductance is a differential-transformer-type inductor formed by winding two spiral inductors. The interdigital capacitor is redesigned and placed inside the inductor to reduce its overall size. With the presence of the digital capacitor, the resonance shifts to the lower frequency, and the amplitude of return loss is increased. The micro-fabricated resonator was realized through integrated passive device technology for sensitive detection and characterization of glucose. The experimental results verified the performance of the proposed biosensor as the radio frequency multi-parameter bio-detector, such as the resonance frequency and the reflection coefficient. The detection results vary in response to deionized water, following by the iterative measurements of the changing glucose concentrations (from 50 to 150 mg$\cdot$dL^{-1}). The concentration of glucose solution changes from 50 mg$\cdot$dL^{-1} to 150 mg$\cdot$dL^{-1}. The experimental results show that the amplitude changes 32.1 dB, and the phase changes 60.88° at 1 GHz. The results indicate the proposed microwave sensor has an excellent biosensing performance.

INDEX TERMS Biosensor, integrated-passive-device fabrication, multi-parameter, glucose detection.

I. INTRODUCTION

Microwave detection is a newly developed technique utilized for characterizing the liquid, solid, gas, or space properties [1], [2], [3], [4]. Its fundamental mechanism can be interpreted by microwave perturbation theory, in which the electromagnetic boundary conditions change with the alteration of the properties of the detected objects, and reflects on the measured microwave parameters, such as transmission or reflection coefficient, resonant frequency, quality factor, etc. [5], [6]. Compared with conventional detection techniques, microwave sensors exhibit unique merits, such as mediator-free [7], label-free [8], high sensitivity [9], non-contact detection [10], ease of integration, etc.

Water [11], [12], [13] is the largest constituent of living and therefore the dielectric properties of water at gigahertz regime

The associate editor coordinating the review of this manuscript and approving it for publication was Norbert Herencsar.

This work is licensed under a Creative Commons Attribution-NonCommercial-NoDerivatives 4.0 License.
For more information, see https://creativecommons.org/licenses/by-nc-nd/4.0/

essentially govern the dielectric properties of biomaterials, such as biological cells, tissues, proteins, skin, blood, and fat [14]. The sensor can be used to characterize the concentration of glucose solution based on the change of dielectric constant of solution Diabetics monitor their health by measuring blood sugar levels. Plenty of studies have presented the evidence that microwave detection could be applied for biomarker detection such as cancer [15], diabetes [16], etc. Besides, other liquid detections such as PH, etc., were also studied. Microwave detection could be quasi-linearly affected by the permittivity and conductivity, as well as the density or properties of the molecules and cells. Conventional biosensors based on the surface plasmon resonance, fluorescence, electro-mechanical transduction, and nanomaterial have been excellently studied for various purposes. They often need sophisticated equipment, labor-intensive sample preparation, or an off-site process for verification of results.

In 1998, Artis et al. developed the earliest form of RF biosensor [17]. The basic detection mechanism is that the resonant frequency and quality factor of a resonator can be determined by the permittivity and permeability of the measuring objects. Since then, the passive-device-based sensors have been extensively researched for biochemical and bio-molecule detection, for example, DNA, proteins, hemoglobin, etc. [18]. According to the operating frequency, the passive-device sensors can be classified into microwave, terahertz, and plasmonic biosensors [19]. The operation of microwave de-vices, including resonator, antenna, resonant cavity, etc., build a stable electromagnetic field with fixed boundary conditions. When a sample is intentionally introduced or the properties of the existing samples change, these boundary conditions will also change, as a result, the transmission and reflection coefficients are changed [20]. The change in resonant frequency is associated with a polarization of the material and the reduction in Q-factor is associated with the dielectric loss of the materials [21].

Compared with the low-temperature cofired ceramic (LTCC) and laminate-embedded passive devices, integrated passive devices (IPDs) offer several improvements including a much smaller chip area, lower cost and power consumption [22], and better compatibility with active devices [23]. IPDs have been widely utilized for passive device fabrication such as filters, baluns, diplexers, and transformers [24], [25]. A chip-on-board (COB) attachment of the RF chips to a printed circuit board (PCBs) is a conventional packaging process, which simplifies the design and manufacturing processes, and results in an improved RF performance for a short interconnection path to eliminate the generation of parasitic parameter [2]. In addition, wire-bonding near a ground plane can reduce radiation loss and increase reliability through improved heat distribution and a small number of solder joints [26].

Therefore, this paper proposed a differential-transformer-type inductor (DTI) intertwined by two spiral inductors, and a redesigned capacitor is connected in parallel to form a new structure with a resonant frequency of 2.4 GHz. The inductive effect of the differential transformer type inductor and the capacitive effect of the redesigned inter-digital capacitor (R-IDC) proposed in this paper allows the resonant unit to operate at lower frequencies, facilitating the miniaturization of the sensor and further improve the quality factor and resolution of the sensor. The IPD process and COB package make the sensor stable and ensure the accuracy of glucose concentration measurement results. This paper consists of the following sections: First, the design and implementation of the IDC and R-IDC structures are proposed, and their capacitive, inductive and resistive effects are analyzed. Then, the sensor fabrication by IPD and the packaging process by COB is explained. Finally, the proposed sensor is utilized to measure the concentrations of glucose solutions, and the experimental results are analyzed and discussed.

II. MATERIALA AND METHODS

Compared with the traditional square inductor (TSI), the resonant frequency of the proposed DTI is lower. The frequency reduction (3.05 GHz to 2.24 GHz) is achieved by parallelly connecting the capacitor in DTI. This plays an important role in limiting the sensor chip size and realizing low monitoring frequency. A low enough operating frequency could avoid background absorption from soft tissue. The soft tissue (human body) limits the penetration depth of electro-magnetic waves if implemented a high frequency. Hence, it's necessary to maintain a small sensor layout while decreasing its operating frequency.

Furthermore, DTI also exhibits better bandpass characteristics than the TSI in the transmission spectra. The existence of shunt capacitance makes the resonant amplitude at the transmission pole further increase (-20.70 dB to -24.73 dB). This is caused by the much higher electric field density, which makes the resonance stronger and leads to a higher Q factor, and in turn, a higher signal-to-noise ratio (SNR). A higher SNR reduces errors in the measurement (e.g., from the network analyzer) and decreases the non-linearity error.

A. THE DT-BASED INDUCTOR

This 4.5-turn square DTI is structured by two separate inductors intertwined using four air-bridge structures, which form the full-differential transformer, as shown in Fig. 1(b). The proposed configuration forms two synchronously tuned coupled resonators with magnetic coupling. It has been verified that the circular and octagonal inductors provide a lower series resistance than the pure square pattern [**?**], [28]db@27a. Besides, there is still the trade-off, in which inductance in unit area achieves the highest value in square design. Therefore, the DTI in this work was designed as a square shape with the bending regions designed as a circular shape. Comparing the simulation results of DTI and TSI, as shown in Fig. 2. The resonant frequency of DTI proposed in this paper is 3.05 GHz, which is much lower than the resonant frequency (8.59 GHz) of TSI The resonant frequency

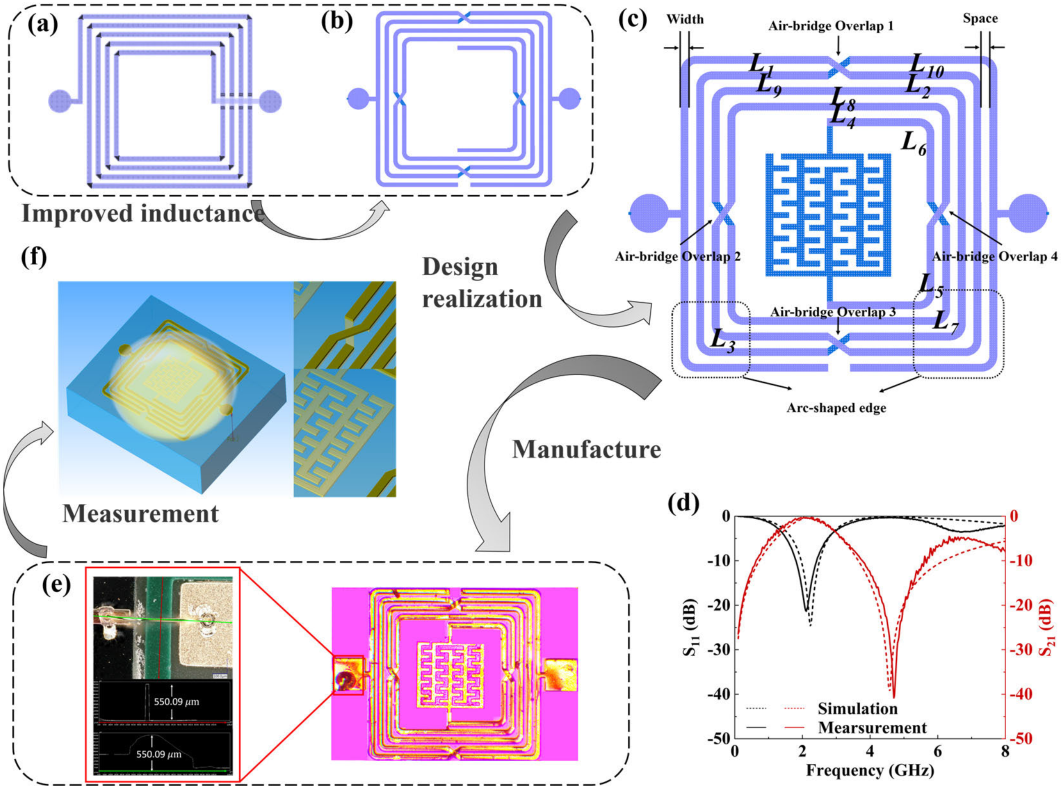

FIGURE 1. (a) Traditional square inductor (TSI), (b) differential transformer type inductor (DTI), (c) RF glucose sensor structure schematic, (d) comparison of glucose sensor's simulation and measurement, (e) microscope photo of glucose sensor(right) and connection pad (left), and (f) glucose solution measurement schematic.

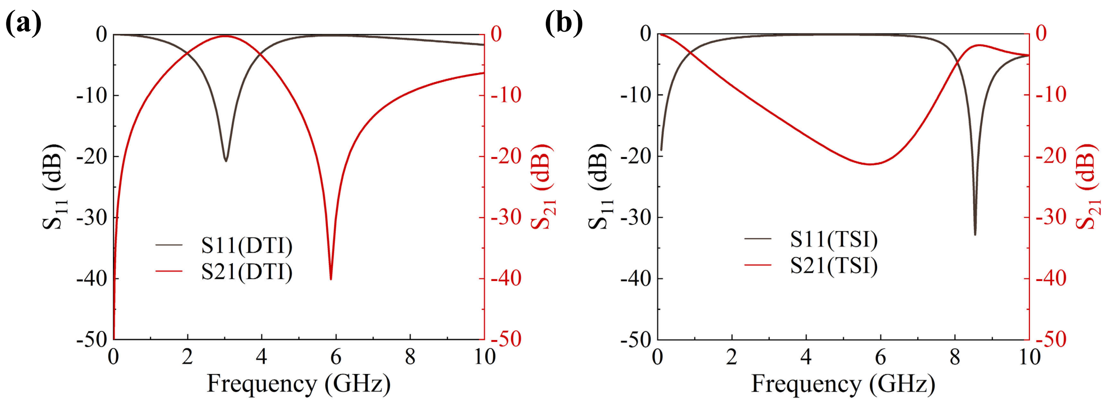

FIGURE 2. Comparison of DTI and TSI's frequency responses (a) DTI, (b) TSI.

can be expressed as:

$$f = \frac{1}{2\pi\sqrt{L_R C_R}} \tag{1}$$

where L_R is the equivalent inductance of DTI, and C_R is the equivalent capacitance of DTI. L_R is related to the self-inductance and mutual inductance of wire. The result indicates that DTI obtains lower resonant frequency under the combined action of equivalent capacitance and equivalent inductance. This design is beneficial to the miniaturization of devices and the enhancement of filling factor. In addition, the lower the resonant frequency, the greater the penetration depth of electromagnetic wave The calculation formula of quality factor is

$$Q = \frac{f_o}{\Delta f_{3\text{dB}}} \tag{2}$$

where f_o is the resonant frequency and $\Delta f_{3\text{dB}}$ is 3dB bandwidth. The calculated quality factor of DTI is 1.59 Q-factor consists of the loaded Q_l, the unloaded Q_u, and the external

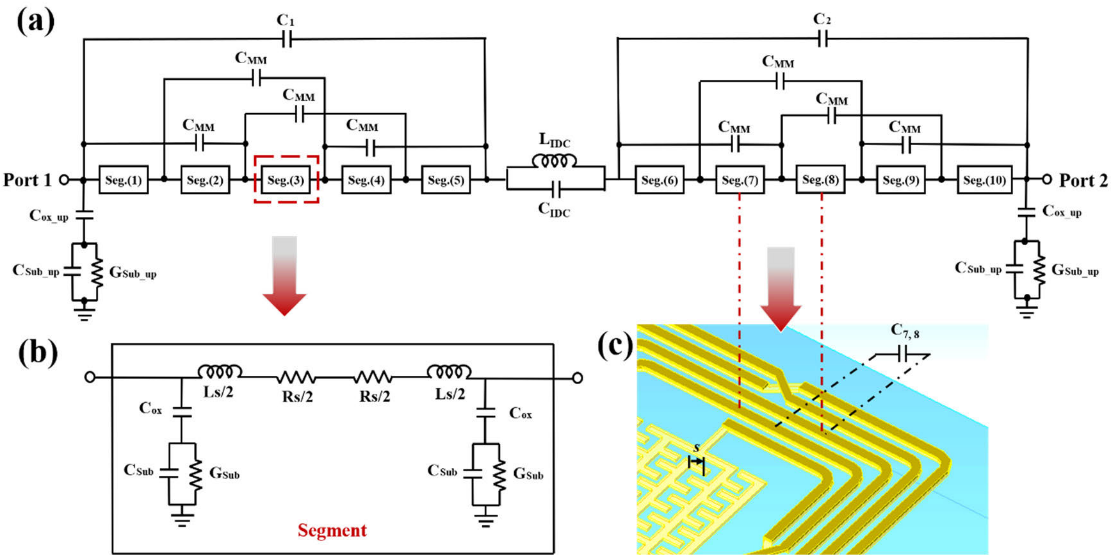

FIGURE 3. (a) The equivalent circuit of the inductor including segments, overlap effect, and capacitive coupling effect, (b) a lumped model of the segment box, and (c) the schematic diagram of plate capacitance effect between inductor lines.

Q_{ext}, in which their relationship is defined as [24]

$$\frac{1}{Q_l} = \frac{1}{Q_u} + \frac{1}{Q_{ext}} \tag{3}$$

Q-factor takes into account both the loading effects of the resonator itself and also the loading of the external circuit. For biosensing, the introduced bio-sample could only affect the Q_{ext}, which finally affected the measured loaded factor. The minimum detectable change in permittivity can be expressed in terms of the loaded Q_l factor of a microwave resonant structure using the following equation:

$$|\Delta\varepsilon_{min}| = \frac{9\sqrt{3}\varepsilon}{2V_{omax}Q_l} \times \sqrt{4kTBR_r} \tag{4}$$

where k is the Boltzmann constant (1.38×10^{-23} m^2 kg s^{-2} K^{-1}), T is the room temperature (°K), B is the bandwidth (Hz), R is the resistance (Ω), ε is the complex permittivity, and V_{omax} is the maximum amplitude of the resonance profile (V).

B. DESIGN TOPOLOGY

As shown in Fig. 1(c), the input and output ports of R-IDC are connected to the L_5 and L_6 inductance lines in DTI, respectively. Increasing the interdigital capacitor structure can increase the unit capacitance and reduce the area so that R-IDC can be connected in parallel inside DTI. Without increasing the area of the sensor chip, the total capacitance of the sensor is increased, and the sensor's performance is improved. R-IDC is a single-layer capacitance structure, which reduces the difficulty of preparation and improves the stability of the sensor. A DTI is in parallel connected with a R-IDC, which formed a LC tank (Fig. 1(c)). For such a pattern, the metal track comprises ten segments as well as four air-bridge overlaps. The equivalent circuit diagram is shown in Fig. 3. The metal lines and their interactions can be represented by capacitance, inductance and resistance effects.

The capacitive effects work as the parasitic effects while consider the chips as a RF chip, which comes from the intercalated finger capacitance effect of R-IDC. Moreover, it comes from the coupling capacitance between metal lines (for example, $C_{7,8}$ in Fig. 3(c)), which includes the capacitance from the air (C_{ca}) and dielectric regions across the coupling gap (C_{cd}).

$$C_{ca} = ln(2\frac{1+\sqrt{\frac{s/k}{s/k+2W/k}}}{1-\sqrt{\frac{s/k}{s/k+2W/k}}}) \tag{5}$$

$$C_{cd} = \frac{\varepsilon_0\varepsilon_r}{\pi}\ln\left[\coth\left(\frac{\pi}{4}\frac{s}{h}\right)\right] + 0.65C_f(\frac{0.02\sqrt{\varepsilon_r}}{\frac{s}{h}} + 1\frac{1}{\varepsilon_r^2}) \tag{6}$$

where s is the metal line space, w is the width of the line, h is the separation between the conductor and the substrate, C_f is the fringe capacitance, ε is the permittivity of free space, and ε_r is the relative permittivity of the dielectric. Thus, the total capacitance of a segment can be calculated as:

$$C_{i,j} = \sum(C_{ca} + C_{cd})(7) \tag{7}$$

The air-bridge structure will show significant capacitive effects. The resistance and inductance effects of the air bridge are ignored because the length of the wire in the air bridge area is much smaller than the whole wire. The capacitance can be calculated as:

$$C_{MM} = \frac{\varepsilon_0(overlap\ area)}{t_{air-bridge}} \tag{8}$$

where ε is the permittivity of the free space and t is the thickness of the air-bridge. For R-IDC, when the interdigital

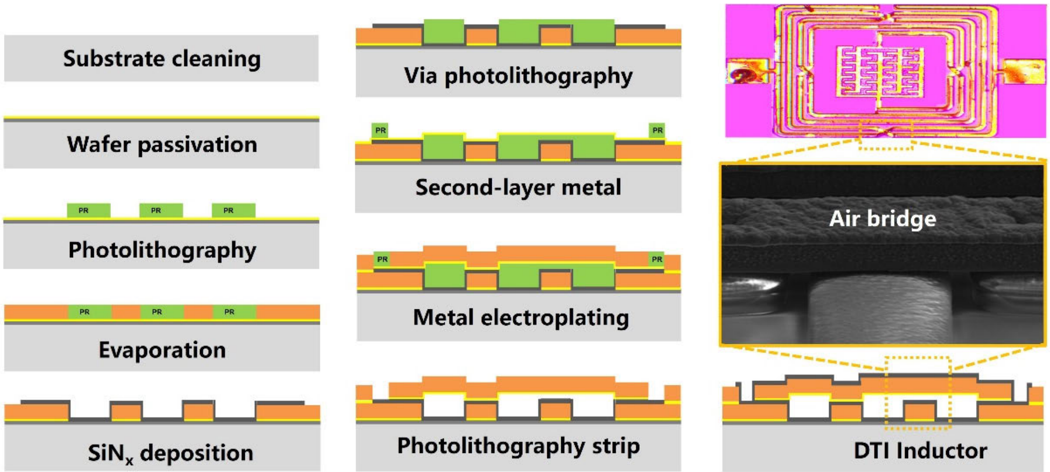

FIGURE 4. The detailed IPD fabrication process.

length is s, the capacitance brought by the interdigital is:

$$C_{IDC} = (\varepsilon_0 + 1)\, s[(N-3)\, \mathrm{A}_1 + \mathrm{A}_2 \tag{9}$$

where N is the number of interdigital pairs. A_1 and A_2 are the internal and external capacitance of IDCs. The inductance effect of the sensor mainly comes from metal lines. For example, inductance line L_4 can be divided into three short and straight metal lines. The inductance value of short and straight metal lines consists of self-inductance L_{si} and mutual inductance L_{mi}. Therefore, the total inductance value of the sensor, L_{di}, can be represented by the sum of inductances of all short straight metal wires.

$$L_{di} = \sum (L_{si} + \sum L_{mi}) \tag{10}$$

The self-inductance of the straight metal line can be expressed as

$$L_{si} = 2(ln\frac{2l}{w_{eff} + t}0.5) \tag{11}$$

where l is the length of the short straight metal line, w_{eff} is the effective linewidth and t is the metal thickness. For the mutual inductance of parallel lines, it can be calculated as:

$$L_{mi} = 2l[\ln\left(\frac{l}{d} + \sqrt{1 + \frac{l^2}{d^2}}\right)\sqrt{1 + \frac{d^2}{l^2}} + \frac{d}{l}] \tag{12}$$

where l is the length of the short straight line and d is the distance between two metal lines. The resistance of the metal line causes the Ohmic loss, which affect the quality of the inductor especially operating at high frequency. The resistance of each metal line can be modeled using the following:

$$R = \frac{\rho \cdot l}{w_{eff} \cdot t_m} \tag{13}$$

where ρ is the resistivity in ohm centimeters, t_m is the metal thickness, and l is the length of the short straight metal line. In addition, C_1 and C_2 in Fig. 3(a) respectively represent the equivalent capacitors of the two parts of DTI, seg. (1) -seg. (10) respectively represent the $L_1 - L_{10}$ ten segment inductor lines, L_{IDC} and C_{IDC} respectively represent the equivalent inductors and capacitors of the R-IDC. The parasitic capacitance effect between metal and ground is represented by C_{ox_up}, and the capacitance and resistance effect of metal ground are represented by C_{sub} and G_{sub}, respectively. Each segment is similarly equivalent to a circuit model formed by series and parallel connections of capacitors, inductors and resistors, as shown in Fig. 3(b).

C. FABRICATION PROCESS

A compound semiconductor GaAs wafer of 6 inch with a thickness of 400 μm was selected as the fabrication substrate. In Fig. 4, the details of IPD fabrication process are described. This type of wafer is highly resistive, and features both a high permittivity of 12.85 F/m and a low loss tangent of 6×10^{-3}, thus being suitable to avoid parasitic effects in high-speed microwave applications.

The process starts with a bottom SiNx deposited by PECVD until a thickness of 2,000 Å is reached. The reason for using a thicker copper layer during the plating process is that Cu has a relatively good conductivity, is easy to solder, enables high-speed operation, and is relatively inexpensive compared to gold. After patterning the resistors and the lower metal cross section of the capacitors and inductors with RIE, 2,000 Å of SiNx was deposited by PECVD as the dielectric intermediate layer The Cu/Au quadratic definition and the plating process are followed by an air-bridge pho-to-process, by which the top electrode and air-bridge are fabricated for the capacitance, and the air-bridge interconnect is formed at the broken loop path around the metal beeline for the inductance. The inductor consists of a metal ring with stacks of the first and second metals and an underpass using only the first metal. Finally, all components are passivated with a thickness of 3000 Å SiNx.

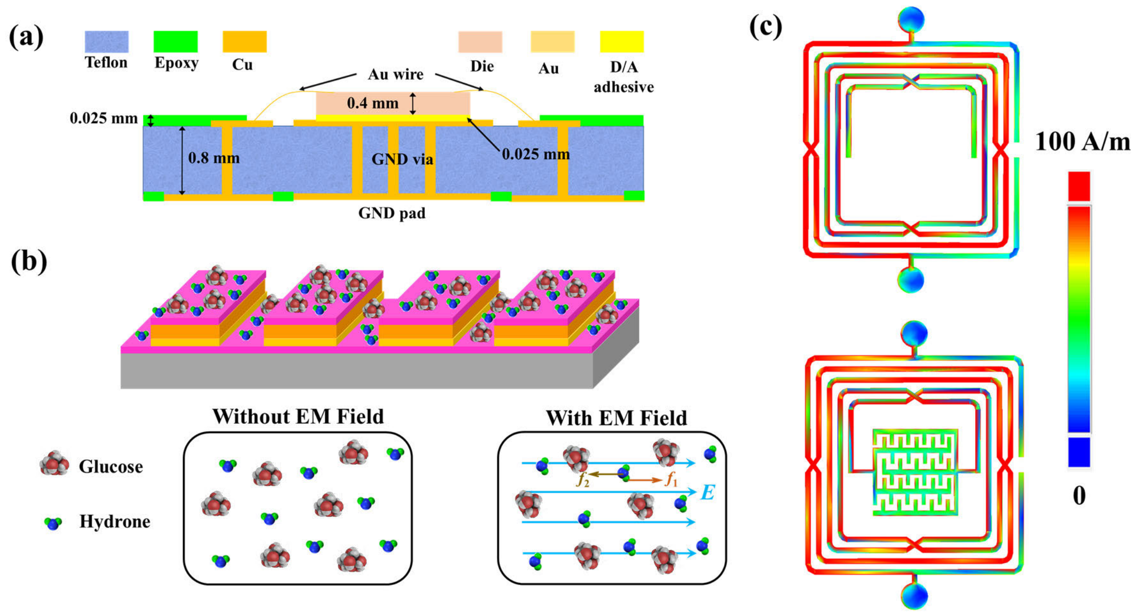

FIGURE 5. (a) COB packaging schematic diagram, (b) glucose and water molecules under electric field force, and (c) simulation diagram of R-IDC used to enhance the current density of DTI.

D. PACKAGING

The main processes of COB packaging include die attaching and wire bonding. The parameters of PCB board and final packaging are shown in Fig. 5. The used PCB has a thickness of 0.8 mm, a dielectric constant of 3.5 and is coated with a 0.025-mm thick epoxy as the passivation layer for device's stability. The back of GaAs substrate is bonded to the copper on the PCB surface using 0.025 mm-thick D/A adhesive for grounding. In addition, the input and output ports of the GaAs device are connected to the two ports on the PCB by a gold wire with a diameter of 0.4 mm bonded to it. The physical picture is shown in Fig. 1(e). The highest point of Au wire measured by electron microscopy with altimetry function is 550.09 μm. The attachment of the die to the PCB simplifies the packaging process and results in improved RF performance for short interconnect paths, which is beneficial for subsequent biosensing. In addition, wire bonding near the ground plane can reduce radiation loss and increase reliability through improved heat distribution and a small amount of solder. Vector Network Analyzer (VNA, N9923, Agilent) is used to measure the packaged biosensor. The VNA is calibrated mechanically and uses N-type calibrators for open circuit, short circuit and load calibration. IF bandwidth is set to 300 Hz. As shown in Fig. 1(d), the simulation results are basically consistent with the measured results. Substrate dielectric losses, metal losses, and fabrication errors contribute to the discrepancy between simulation and measurement, as well as to the difference between the return loss and the resonance frequency [29].

III. RESULTS

A pipette was used to drop the glucose solution above the sensor for quantitative detection of glucose concentration, as shown in Fig. 1(f). The volume of solution sample used for each measurement is 0.70 μL. In order to ensure that the error of each measurement is as small as possible, the following three main efforts are made. First, the appropriate sample measurement volume is selected. When 0.70 μL solution is dropped on the surface of the device, it can completely cover the surface of the device, and can aggregate into droplets due to the effect of liquid surface tension. Secondly, the overall size of the device is small, which is 1070 μm * 810 μm. The 0.7 μL sample can fully cover the device, which reduces the impact of sample position migration. Finally, standardized operation procedures are strictly used in the measurement process.

The measured temperature and relative humidity of the individual samples ranged from 22.1 °C to 22.6 °C and 14.1–14.3%, respectively. After RF measurement of a sample, the backside slot and front-side tank were flushed several times first with phosphate-buffered saline (1x PBS, pH = 7.4, consisting of 137 mmol/L NaCl, 2.7 mmol/L KCl, 10 mmol/L Na_2HPO_4, and 2 mmol/L KH_2PO_4, prepared by the Department of Biochemistry and Molecular Biology, Medical College, KyungHee University, Seoul, S. Korea) and then with DI water to remove the glucose sample prior to measuring the next sample. Finally, the DI water was cleaned with KIMTECH science wipers and the biosensor was ready for the next measurement. Subsequently, the excitation signal passes through the glucose solution at the transmitter end and reaches the receiver end, to obtain the S parameter at different frequencies. Then, the glucose concentration value can be obtained by combining the established model with the calculated parameter information. The RF signal is attenuated during the measurement process, as shown in Fig. 6. After the incident wave (a1) passes through the

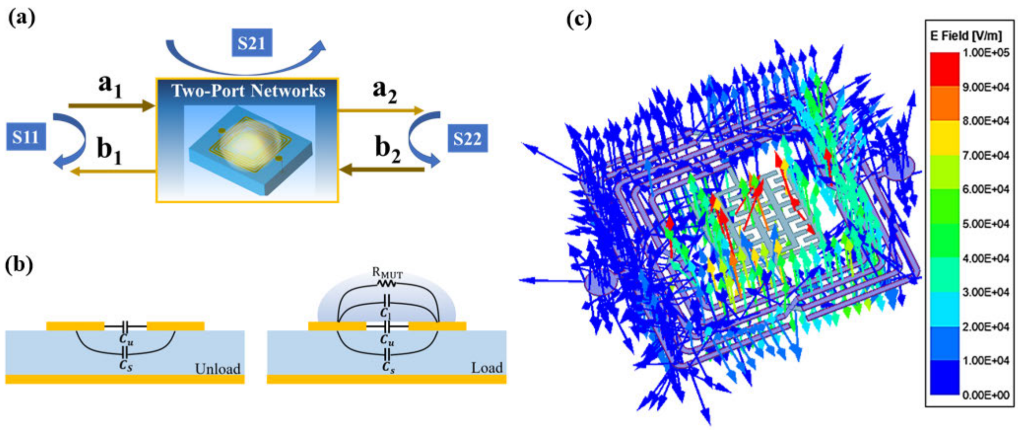

FIGURE 6. (a) Linear two-port network, (b) equivalent circuit of the bare chip (top figure) and after the introduction of the sample (bottom figure), (c) electric field radiation pattern.

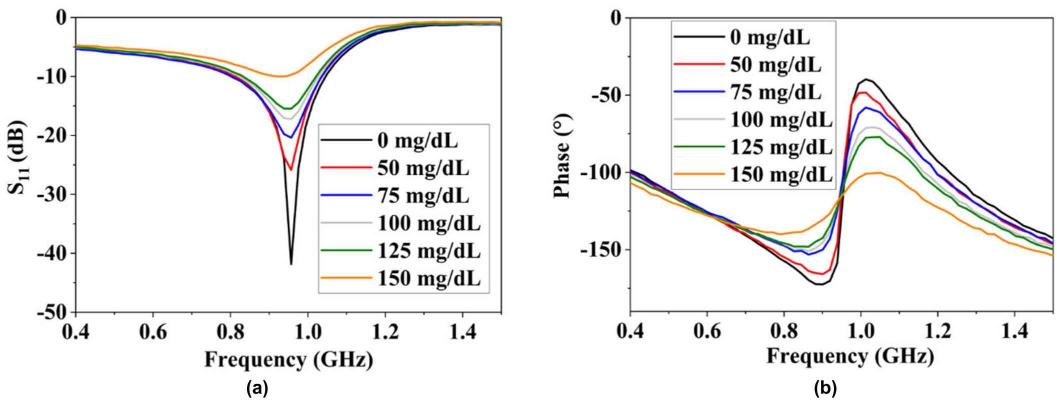

FIGURE 7. (a) Reflection amplitude spectrum changes, and (b) phase changes under glucose solutions concertation from 0-150 mg/dL.

two-port network, part of the signal is reflected to (b1), and part of the signal passes through the network and becomes the outgoing wave (a2). Similarly, when considered from the right side, the matrix equation of S parameter is shown in Equation (12). So, the reflection coefficient S_{11} is used to characterize the reflection signal in a two-port network.

$$\begin{bmatrix} b_1 \\ b_2 \end{bmatrix} = \begin{bmatrix} S_{11} & S_{12} \\ S_{21} & S_{22} \end{bmatrix} \begin{bmatrix} a_1 \\ a_2 \end{bmatrix} \tag{14}$$

The spatial electric field simulation results of RF biosensor are shown in Fig. 6(c). The results show that the electric field is mainly concentrated in R-IDC and air bridge region. Samples of D-glucose aqueous solution consisting of a mixture of DI water and D-glucose powder were prepared at five concentrations: 50, 75, 100, 125, and 150 mg/dL. The electromagnetic field passes through the glucose solution, and the solution absorbs the energy of the electromagnetic field, which varies with the glucose concentration. To reduce errors, the samples were kept at the same temperature before testing and were washed with deionized water after each test and then dried before the next test. In the glucose concentration test, the glucose concentration was increased by 25 mg/dL each time from 50 mg/dL to 150 mg/dL. The molecules in a material consist of symmetrically distributed positive and negative charges, where the molecular electric dipole moment is zero and is electrically neutral from an overall perspective. Under the action of an applied electric field, the electron cloud distributed around the nucleus is shifted by the electric field force, thus forming an electric dipole. When the positively and negatively charged centers do not coincide, such as hydrogen ions, the molecule can be regarded as an electric dipole consisting of a pair of positive and negative charges close to each other. When the electric field is present, the chaotic polar molecules appear to be arranged in a regular manner, resulting in orientated polarization. Under the action of an external electric field, the electric field force (f_1) causes the intrinsic dipole moment of the molecules to tend to be distributed in the direction of the electric field lines, while the interactions between the molecules and their own thermal motion will impede this arrangement, which is expressed as a force (f_2) in the opposite direction compared to the electric field force. In this case, the molecular arrangement tends to be regular, as shown in Fig. 5(b). With time, changes in the electric field cause the electric dipole to move in simple

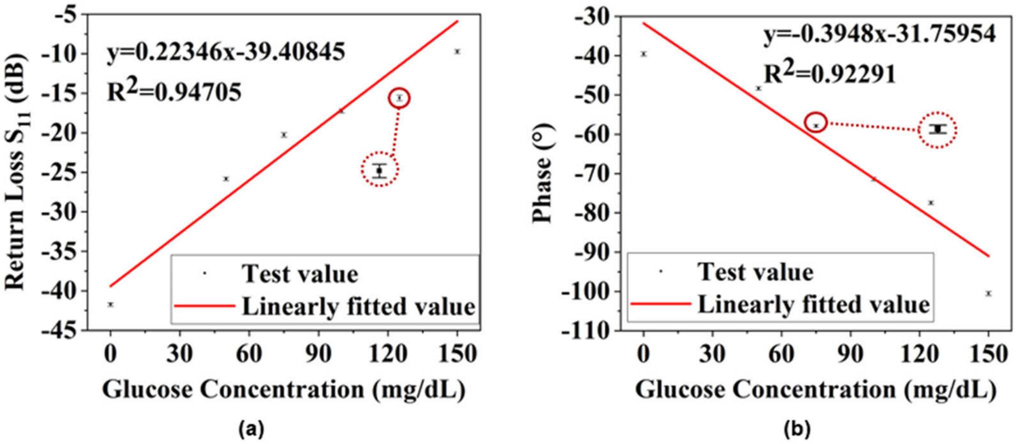

FIGURE 8. (a) Amplitude variation of return loss, and (b) phase variation at 1 GHz.

harmonic motion. The effect of the electromagnetic wave excited by the dipole during this process on the overall electro-magnetic field can be characterized by the macroscopic dielectric constant. Glucose has relaxation and dispersion properties, which are frequency dependent. The frequency dependence of the complex permittivity in the RF range can be determined from the Cole-Cole relationship.

$$\varepsilon = \varepsilon' - j\varepsilon'' = \varepsilon_\infty + \frac{\varepsilon_s - \varepsilon_\infty}{1 + (j\omega/\omega_0)^{1-\alpha}} \tag{15}$$

where ε_s is the static complex dielectric constant, ε_∞ is the optical frequency com-plex dielectric constant, $\omega_0/2\pi$ is the Debye relaxation frequency and α is the Cole-Cole factor. The real and imaginary parts of the complex permittivity can be formulated in the Debye model [9].

$$\varepsilon'(\omega) = \varepsilon_\infty + \frac{\varepsilon_s - \varepsilon_\infty}{1 + \omega^2\tau^2} \tag{16}$$

$$\varepsilon''(\omega) = \frac{(\varepsilon_s - \varepsilon_\infty)\omega\tau}{1 + \omega^2\tau^2} \tag{17}$$

where $\omega = 2\pi f$, $\tau = 1/2\pi f_R$. f_R is the relaxation frequency. In this paper, Debye equation is used to calculate the dielectric constant of glucose solutions with different concentrations, and the results are shown in Fig. 9

The results of the R-IDC test are shown in Fig. 7. As the glucose concentration increases, the amplitude of S_{11} increases from -41.83 dB to -9.73 dB, a change of 32.1 dB The variation of S11 amplitude is caused by dielectric loss, which is mainly composed of conductance loss, polarization loss and ionization loss. They are caused by leakage current, dipole rearrangement and partial discharge. Under the action of electric field, as the concentration of glucose solution increases, the absolute value of return loss amplitude gradually decreases, that is, the loss increases with the increase of glucose solution concentration. At the same time the phase at 1 GHz decreases from -39.69° to -100.57°, a change of 60.88°. Phase is the integral of frequency over time. The phase at the same frequency reflects the response time

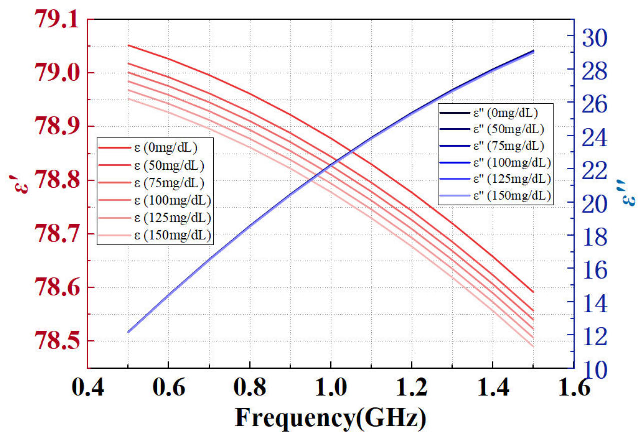

FIGURE 9. Permittivity of glucose solutions with different concentrations.

of the whole system. In different concentrations of glucose solution, the time required to establish the internal electric field is also different, which is macroscopically manifested as phase change. In addition, the degree of phase reversal is related to the coupling state of the sensor. The different concentration of glucose solution affects the coupling degree of the sensor. The analysis showed a good linear correlation between the glucose concentration and the amplitude change and phase shift of S_{11}, as shown in Fig. 8(a) and (b). The linear regression equation corresponding to the change in amplitude of S11 for glucose concentration is shown below.

$$y_1\,(\mathrm{dB}) = 0.20137x\,(\mathrm{mg/dL}) - 38.52214 \tag{18}$$

linear correlation $R^2 = 0.94389$.

The linear regression equation corresponding to the glucose concentration and the phase shift is as follows.

$$y_2\,(^\circ) = -0.39255x\,(\mathrm{mg/dL}) - 33.15929 \tag{19}$$

linear correlation $R^2 = 0.92547$.

The y_1 and y_2 are the amplitude and phase of S_{11}, respectively, and x is the concentration of glucose solution. The results show that the sensor can be used for glucose detection and that the amplitude and phase of S_{11} show a good linear relationship with the glucose level in the range of 50 mg/dL - 150 mg/dL, enabling a multi-parameter characterization of glucose levels. The sensing limitation of the proposed devices, known as the limit of detection (LOD) [31], was calculated on the basis of following equation as 4.1 mg/dL and 3.8 mg/dL, respectively.

$$LOD = 3.3 \times SD/m \tag{20}$$

where SD is the standard deviation of the Return Loss S_{11} and the Phase at 1 GHz, and m is the slope of the regression line. The nature of the calibration curves and the data obtained from the Return Loss S_{11} and the Phase at 1 GHz shifted with a relative standard deviation (RSD) of less than 1% for the RF biosensor, indicating a small spread of the Return Loss S_{11} and the Phase at 1 GHz for a particular concentration.

As shown in Fig. 7(a), changing the concentration of the glucose solution, the resonant frequency of the sensor is almost constant, while the amplitude of S_{11} varies linearly for the following reasons. From Fig. 5(c) it can be seen that the presence of the R-IDC increases the current density in the internal loop of the DTI so that the inductive effect is enhanced. The glucose solution loaded on the sensor mainly affects the air bridge capacitance and the capacitance formed by the R-IDC and the air in the electric field above, as shown in Fig. 5(b). The sensor uses a GaAs substrate, which makes the value of the substrate capacitance much larger than the capacitance of the two parts affecting the sensing effect, and the total capacitance of the sensor is larger as shown by the capacitance analysis in the previous chapter. Therefore, the glucose solution has almost no effect on the total capacitance C, and the corresponding resonant frequency of the sensor is almost constant.

IV. CONCLUSION

This paper presents an IPD-based LC RF sensor designed for glucose solution sensing. Using a TSI as a prototype, a DTI combined with a shaped interpolated finger capacitor are utilized to reduce the resonant frequency and increase the resonant amplitude to further improve the sensing resolution, which can be used for glucose solution sensing. RF sensors in COB packages shows excellent sensing performance for glucose solutions of 50 mg/dL - 150 mg/dL. The sensor works at lower frequencies and its electromagnetic waves can penetrate skin tissue. In the next practical application process, the sensor can be directly attached to the skin surface for non-contact monitoring of blood components. Moreover, when multiple RF sensors are used to form an array, the angiography of subcutaneous tissue can be further realized.

ACKNOWLEDGMENT

(Jia-Kang Wu and Jun-Ge Liang contributed equally to this work.)

REFERENCES

[1] J.-K. Wu, K. Gao, W. Yue, T. Qiang, N.-Y. Kim, W. Song, X.-F. Gu, S. von Gratowski, and J.-G. Liang, "A way to determine the optimum detection frequency for microwave sensing," *Measurement*, vol. 202, Oct. 2022, Art. no. 111736.

[2] W. Yue, E.-S. Kim, B.-H. Zhu, J. Chen, J.-G. Liang, and N.-Y. Kim, "Permittivity-inspired microwave resonator-based biosensor based on integrated passive device technology for glucose identification," *Biosensors*, vol. 11, no. 12, p. 508, Dec. 2021.

[3] Y. Ma, T. Qiang, M. Gao, J. Liang, and Y. Jiang, "Quantitative, temperature-calibrated and real-time glucose biosensor based on symmetrical-meandering-type resistor and intertwined capacitor structure," *Biosensors*, vol. 11, no. 12, p. 484, Nov. 2021.

[4] M. Gao, T. Qiang, Y. Ma, J. Liang, and Y. Jiang, "RFID-based microwave biosensor for non-contact detection of glucose solution," *Biosensors*, vol. 11, no. 12, p. 480, Nov. 2021.

[5] I. Rusni, A. Ismail, A. Alhawari, M. Hamidon, and N. Yusof, "An aligned-gap and centered-gap rectangular multiple split ring resonator for dielectric sensing applications," *Sensors*, vol. 14, no. 7, pp. 13134–13148, Jul. 2014.

[6] X. Wang, J.-G. Liang, J.-K. Wu, X.-F. Gu, and N.-Y. Kim, "Microwave detection with various sensitive materials for humidity sensing," *Sens. Actuators B, Chem.*, vol. 351, Jan. 2022, Art. no. 130935.

[7] K. K. Adhikari and N. Kim, "Ultrahigh-sensitivity mediator-free biosensor based on a microfabricated microwave resonator for the detection of micromolar glucose concentrations," *IEEE Trans. Microw. Theory Techn.*, vol. 64, no. 1, pp. 319–327, Jan. 2016.

[8] H. Park, H. Seo Yoon, U. Patil, R. Anoop, J. Lee, J. Lim, W. Lee, and S. Chan Jun, "Radio frequency based label-free detection of glucose," *Biosensors Bioelectron.*, vol. 54, pp. 141–145, Apr. 2014.

[9] T. Qiang, C. Wang, and N.-Y. Kim, "Quantitative detection of glucose level based on radiofrequency patch biosensor combined with volume-fixed structures," *Biosensors Bioelectron.*, vol. 98, pp. 357–363, Dec. 2017.

[10] M. H. Zarifi, P. Shariaty, Z. Hashisho, and M. Daneshmand, "A non-contact microwave sensor for monitoring the interaction of zeolite 13X with CO_2 and CH_4 in gaseous streams," *Sens. Actuators B, Chem.*, vol. 238, pp. 1240–1247, Jan. 2017.

[11] O. Korostynska, M. Ortoneda-Pedrola, A. Mason, and A. I. Al-Shamma'a, "Flexible electromagnetic wave sensor operating at GHz frequencies for instantaneous concentration measurements of NaCl, KCl, $MnCl_2$ and CuCl solutions," *Meas. Sci. Technol.*, vol. 25, no. 6, Jun. 2014, Art. no. 065105.

[12] K. Zhang, R. K. Amineh, Z. Dong, and D. Nadler, "Microwave sensing of water quality," *IEEE Access*, vol. 7, pp. 69481–69493, 2019.

[13] S. Oh, I. Hossen, J. Luglio, G. Justin, J. E. Richie, H. Medeiros, and C. H. Lee, "On-site/in situ continuous detecting ppb-level metal ions in drinking water using block loop-gap resonators and machine learning," *IEEE Trans. Instrum. Meas.*, vol. 70, pp. 1–9, 2021.

[14] G. Guarin, M. Hofmann, J. Nehring, R. Weigel, G. Fischer, and D. Kissinger, "Miniature microwave biosensors: Noninvasive applications," *IEEE Microw. Mag.*, vol. 16, no. 4, pp. 71–86, May 2015.

[15] Z. Geng, X. Zhang, Z. Fan, X. Lv, and H. Chen, "A route to terahertz metamaterial biosensor integrated with microfluidics for liver cancer biomarker testing in early stage," *Sci. Rep.*, vol. 7, p. 16378, Nov. 2017.

[16] N.-Y. Kim, K. K. Adhikari, R. Dhakal, Z. Chuluunbaatar, C. Wang, and E.-S. Kim, "Rapid, sensitive and reusable detection of glucose by a robust radiofrequency integrated passive device biosensor chip," *Sci. Rep.*, vol. 5, no. 1, pp. 1–9, Jan. 2015.

[17] F. Artis, T. Chen, T. Chretiennot, J. Fournie, M. Poupot, D. Dubuc, and K. Grenier, "Microwaving biological cells: Intracellular analysis with microwave dielectric spectroscopy," *IEEE Microw. Mag.*, vol. 16, no. 4, pp. 87–96, May 2015.

[18] G. Manasa, R. J. Mascarenhas, N. P. Shetti, S. J. Malode, A. Mishra, S. Basu, and T. M. Aminabhavi, "Skin patchable sensor surveillance for continuous glucose monitoring," *ACS Appl. Bio Mater.*, vol. 5, no. 3, pp. 945–970, Mar. 2022.

[19] T. Chen, S. Li, and H. Sun, "Metamaterials application in sensing," *Sensors*, vol. 12, no. 3, pp. 2742–2765, Feb. 2012.

[20] X. Fu, J. Wu, X. Wang, X. Gu, C. Wang, Y. Wu, and J. Liang, "NSRR microwave sensor based on PLL technology for glucose detection," *IEEE Trans. Microw. Theory Techn.*, vol. 71, no. 2, pp. 763–772, Feb. 2023.

[21] A. Salim and S. Lim, "Review of recent metamaterial microfluidic sensors," *Sensors*, vol. 18, no. 1, p. 232, Jan. 2018.

[22] T. Qiang, C. Wang, M.-Q. Liu, K. K. Adhikari, J.-G. Liang, L. Wang, Y. Li, Y.-M. Wu, G.-H. Yang, F.-Y. Meng, J.-H. Fu, Q. Wu, N.-Y. Kim, and Z. Yao, "High-performance porous MIM-type capacitive humidity sensor realized via inductive coupled plasma and reactive-ion etching," *Sens. Actuators B, Chem.*, vol. 258, pp. 704–714, Apr. 2018.

[23] C. Wang, W. S. Lee, F. Zhang, and N. Y. Kim, "A novel method for the fabrication of integrated passive devices on Si-GaAs substrate," *Int. J. Adv. Manuf. Technol.*, vol. 52, nos. 9–12, pp. 1011–1018, Feb. 2011.

[24] J. Liang, C. Wang, and N. Kim, "Integrated passive device fabricated and chip-on-board packaged filter employing mixed electric-magnetic coupling scheme," *IET Microw., Antennas Propag.*, vol. 12, no. 14, pp. 2191–2198, Nov. 2018.

[25] Y. Li, C. Wang, and N. Kim, "Design of very compact bandpass filters based on differential transformers," *IEEE Microw. Wireless Compon. Lett.*, vol. 25, no. 7, pp. 439–441, Jul. 2015.

[26] H. Yu, J.-G. Liang, C. Wang, C.-C. Liu, B. Bai, F.-Y. Meng, D.-Q. Zou, L. Ali, C.-Q. Jing, M. Zhao, L. Wang, and X.-F. Gu, "Target properties optimization on capacitive-type humidity sensor: Ingredients hybrid and integrated passive devices fabrication," *Sens. Actuators B, Chem.*, vol. 340, Aug. 2021, Art. no. 129883.

[27] C. Wang and N. Y. Kim, "Analytical optimization of high-performance and high-yield spiral inductor in integrated passive device technology," *Microelectron. J.*, vol. 43, no. 3, pp. 176–181, Mar. 2012.

[28] J. Lee, K. A. Hyun, and H. Jung, "A high-Q resonator using biocompatible materials at microwave frequencies," *Appl. Phys. Lett.*, vol. 104, no. 2, Jan. 2014, Art. no. 023509.

[29] K. Gao, J. Wu, X. Wang, N. Kim, X. Gu, and J. Liang, "Specific detection of organic and inorganic solution based on microwave resonator array," *IEEE Sensors J.*, vol. 22, no. 11, pp. 10532–10540, Jun. 2022.

JIA-KANG WU was born in Huanggang, Hubei, China, in 1995. He received the B.Eng. degree in electronic and information engineering from Northeastern University, in 2019. He is currently pursuing the Ph.D. degree in IoT engineering and technology with Jiangnan University. His research interests include design and development of radio frequency and microwave devices and humidity sensors.

YING-YING JI is currently a Doctor with Wuxi Central Rehabilitation Hospital, The affiliated Wuxi Mental Health Center, Jiangnan University.

JUN-GE LIANG was born in Yantai, Shandong, China, in 1991. He received the Ph.D. degree in electronic engineering from Kwangwoon University, South Korea, in 2018. He is currently an Associate Professor with Jiangnan University, Wuxi, China. His research interest includes microwave devices. He has been a reviewer of IEEE Transactions on Components, Packaging and Manufacturing Technology and *IET Electronics Letters*.

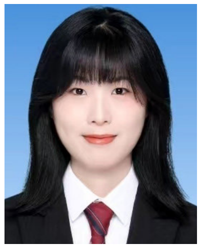

YU-TING CHEN was born in Heze, Shandong. She received the bachelor's degree from the University of Jinan, in 2020. She is currently pursuing the master's degree with Jiangnan University. Her research interests include microwave sensors and radio frequency circuits.

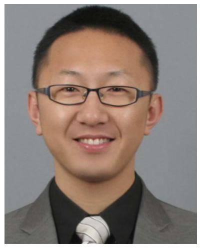

CONG WANG was born in Qingdao, Shandong, China, in 1982. He received the B.S. degree in automation engineering from Qingdao Technological University, Qingdao, in 2005, and the M.S. and Ph.D. degrees in electronic engineering from Kwangwoon University, Seoul, South Korea, in 2008 and 2011, respectively.

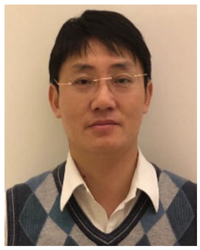

CHENG QIAN received the B.S. degree in automation engineering from Northeast University, China, in 2003, the M.S. degrees in electrical engineering from Kwangwoon University, South Korea, in 2008. He is currently pursuing the Ph.D. degree in electrical engineering with the University of Zhejiang, China.

YANG-FAN SUN is currently a Doctor with Wuxi Central Rehabilitation Hospital, The affiliated Wuxi Mental Health Center of Jiangnan University.

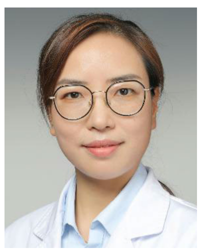

CAI-LI REN received the M.D. degree with specializes in wearable devices and brain regulation.

SVETLANA VON GRATOWSKI received the Ph.D. degree from the Science Institute of Radio Engineering and Electronics, Academy of Science USSR. She is currently with the Institute of Radio Engineering and Electronics, Russian Academy of Sciences (IRE RAS). Her research interests include theoretical physics in magnetism, magnetic domains, and electromagnetic waves properties of condensed matter.